ARTICLE

Mutually Noninterfering Flexible Pressure–Temperature Dual-Modal Sensors Based on Conductive Metal–Organic Framework for Electronic Skin

Yuxiang Li, Ranran Wang,* Guan-E Wang,* Shiyang Feng, Wenge Shi, Yin Cheng, Liangjing Shi, Kaiyuan Fu, and Jing Sun*

Read Online

ACCESS | Metrics & More | Article Recommendations | SI Supporting Information

ABSTRACT: Pressure and temperature are two important indicators for human skin perception. Electronic skin (E-skin) that mimics human skin within one single flexible sensor is beneficial for detecting and differentiating pressure and temperature and showing immunity from tensile strain disruptions. However, few studies have simultaneously realized these conditions. Herein, a flexible and strain-suppressed pressure–temperature dual-modal sensor based on conductive and microstructured metal–organic framework (MOF) films was reported and mainly prepared by *in situ* growing $Ni_3(HiTP)_2$ onto microstructured mixed cellulose (MSMC) substrates. The sensor exhibits distinguishable and strain-suppressed properties for pressure (sensing range up to 300 kPa, sensitivity of 61.61 kPa^{-1}, response time of 20 ms, and ultralow detection limit of 1 Pa) and temperature sensing (sensitivity of 57.1 μV/K). Theoretical calculations successfully analyzed the mutually noninterfering mechanism between pressure and temperature. Owing to its effective perception in static and dynamic surroundings, this sensor has great potential applications, such as in electronic skin and smart prosthetics.

KEYWORDS: conductive metal−organic framework, flexible sensor, pressure−temperature sensing, mutually noninterfering, tensile strain suppression
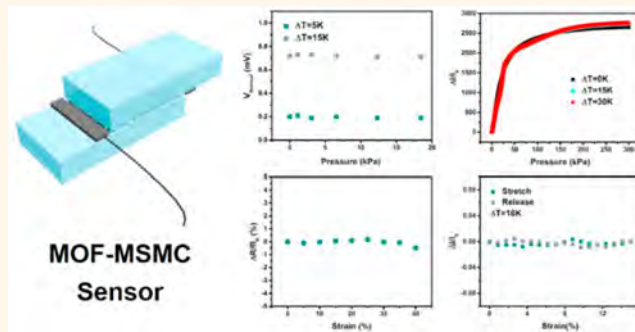
H uman skin[1] is one of the most important somatosensory systems of the body because it contains many receptors[2] for sensing and distinguishing multiple stimuli.[3] Mimicking and even surpassing the sensing properties of human skin,[4] electronic skin (E-skin) is anticipated to play an important role in personal healthcare,[5] human−machine interaction,[6] soft robotics,[7] and other fields[8,9] due to its abundant flexible and receptor-like sensors.[10,11] Pressure[12] and temperature[13] are two crucial parameters for human skin perception. For the development of E-skin, on one hand, E-skin requires flexible sensors to distinctively sense pressure and temperature.[14] On the other hand, both sensing processes should be immune to other external stimuli, such as frequent stretching from human daily activities.[15]

Previously, the pressure−temperature dual function of E-skin has been realized by integrating various single-function sensors[16,17] or by means of theoretical calibration.[18,19] However, these E-skins have complex configurations or algorithms, and

the sensing outputs are usually inaccurate because of the mutual interference between pressure/temperature signals and external disruptions from tensile strain. To tackle these issues, one solution is to fabricate one single flexible dual-modal sensor by using advanced sensing materials that respond to pressure and temperature but are insensitive to tensile strain. Currently, some flexible pressure−temperature dual-modal sensors have been constructed using these sensing materials, however these sensors cannot successfully realize mutually undisturbed pressure− temperature dual-sensing functions[20,21] or suppress stretch interruptions.[22−25] For example, the most commonly used
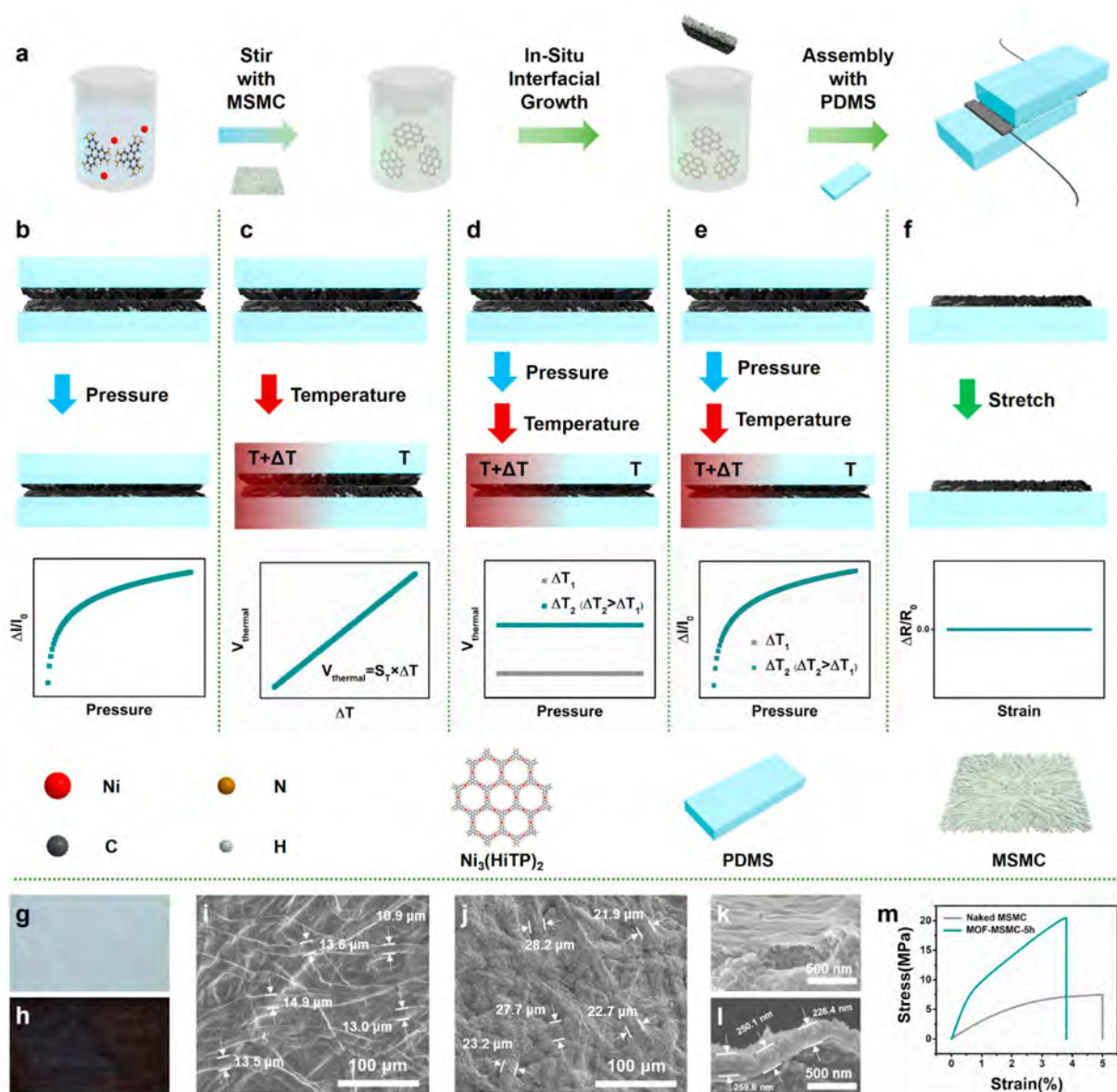
Figure 1. Schematic of the preparation, sensing mechanisms, and characterizations of the MOF-MSMC sensor. (a) Preparation process of the MOF-MSMC sensor. (b) Schematic diagrams of the response mechanism of the MOF-MSMC sensor under pressure stimulation. (c) Schematic diagrams of the response mechanism of the MOF-MSMC sensor under temperature stimulation. (d, e) Schematic diagrams of the response mechanism of the MOF-MSMC sensor under simultaneous pressure and temperature stimulation. (f) Schematic diagrams of the response mechanism of one part of the MOF-MSMC sensor under stretch stimulation. (g) Optical image of the naked MSMC. (h) Optical image of the MOF-MSMC-5h composite film. (i) Top-view SEM morphology of the naked MSMC. (j) Top-view SEM morphology of the MOF-MSMC-5h composite film. (k) Cross-sectional SEM morphology of the naked MSMC. (l) Cross-sectional SEM morphology of the MOF-MSMC-5h composite film. (m) Stress *versus* strain curves of the naked MSMC substrate and the MOF-MSMC-5h composite film.

pressure−temperature dual-modal sensors are poly(3,4-ethylenedioxythiophene):poly(styrenesulfonate) (PE-DOT:PSS)-based aerogels,[22,24,25] which however have low sensitivity (4.6 kPa^{-1}) and narrow sensing range (up to 20 kPa) and cannot suppress strain interruptions.[22] Yang *et al.*[20] proposed a BaTiO$_3$ based dual-modal sensor that can simultaneously detect pressure and temperature. However, it can hardly discriminate temperature sensing from pressure sensing due to the pyro-piezoelectricity coupling effect of BaTiO$_3$. Bao and co-workers[23] presented a creative method to differentiate mechanical and thermal information based on ion relaxation dynamics, but the mixture of pressure and stretch in

the mechanical information hinders the precise perception of the pressing event.

Recent years have witnessed rapid progress of metal−organic frameworks (MOFs). Compared with other conductive materials such as metal nanowires, carbon nanotubes, graphene, and MXenes, MOFs possess the merit of designable micro-structures[26] that renders them potential sensing materials for constructing a dual-modal sensor satisfying the requirements mentioned above. However, because of the low conductivity of most MOFs, the difficult preparation of continuous and stable conductive MOF films with designable microstructures,[27] and the difficulty of conductive MOF films in suppressing tensile strain, there still have been no reports concerning MOF
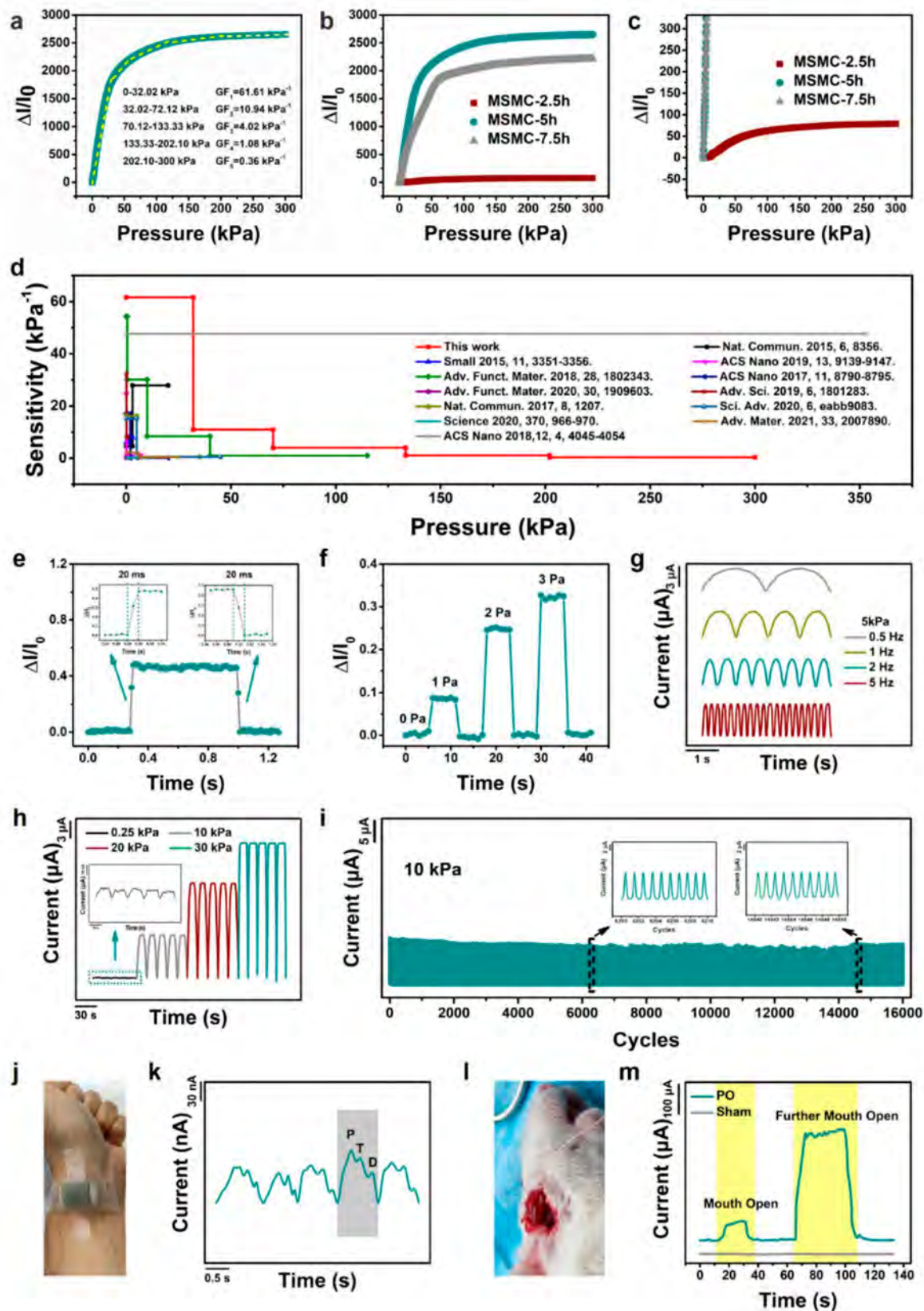
Figure 2. Pressure-sensing behaviors of MOF-MSMC sensors. (a) Relative current variation *versus* pressure curve of the MOF-MSMC-5h sensor. **(b)** Relative current variation *versus* pressure curves of MOF-based sensors with various growth time (2.5, 5, and 7.5 h). **(c)** Enlarged reproduction of the curves in **(b)** within relative current variation from 0 to 325. **(d)** Comparison of the relationship between sensitivity and pressure-sensing range of the MOF-MSMC-5h sensor with previously reported studies. **(e)** Relative current variation of the MOF-MSMC-5h sensor under a sudden pressure stimulus. Insets illustrate the response (left) and recovery time (right), respectively. **(f)** Relative current

Figure 2. continued

variation of the MOF-MSMC-5h sensor under gradually increasing pressure from 1 Pa to 3 Pa. (g) Current variation of the MOF-MSMC–5h sensor at selected frequencies under 5 kPa. (h) Current variation of the MOF-MSMC-5h sensor under gradually increasing pressure from 0.25 kPa to 30 kPa. The inset illustrates the current variation under five successive input pressure steps of 0.25 kPa. (i) Current variation of the MOF-MSMC-5h sensor under a pressure of 10 kPa up to 16 000 cycles. The insets illustrate the sensor under input pressure steps from the 6200th to the 6210th (left) and from the 14540th to the 14550th (right). (j) Optical image of the MOF-MSMC-5h sensor adhered onto the wrist. (k) Current variation of the MOF-MSMC-5h sensor under periodic stimuli from pulse waves. (l) Optical image of the MOF-MSMC-5h sensor embedded between the temporomandibular anterior joint disk and the condyle of a rat. (m) Current variation of the MOF-MSMC-5h sensor under pressure stimulation due to the displacement of the temporomandibular joint disk resulting from the rat opening its mouth. Sham denotes the rat without temporomandibular anterior joint disk displacement when it is opening its mouth, and PO represents the rat possessing temporomandibular anterior joint disk displacement when it is opening its mouth.

materials based flexible and strain-suppressed pressure−temperature dual-modal sensors.

Herein, a flexible strain-suppressed pressure−temperature dual-modal sensor based on microstructured and highly conductive MOF films was proposed and mainly prepared by *in situ* growing $Ni_3(HiTP)_2$[28,29] onto microstructured mixed cellulose (MSMC) substrates. This sensor exhibits good pressure-sensing performance (broad sensing range up to 300 kPa, high sensitivity of 61.61 kPa^{-1}, short response time of 20 ms, and ultralow detection limit of 1 Pa) that surpasses most dual-modal sensors.[16,22,24,25,30,31] Its temperature-sensing properties (high sensitivity of 57.1 $\mu V/K$ and low hysteresis effect) are also good compared with PEDOT:PSS-,[24] graphene-,[31] and MXene-AgNW-PEDOT:PSS-PP:TeNW-based dual-modal sensors.[32] Additionally, its sensing functions for pressure and temperature are mutually noninterfering, the mechanism of which is successfully disclosed from the perspective of material science through theoretical calculations. The tensile Young's modulus of the MOF-MSMC composite film is larger than that of polydimethylsiloxane (PDMS). As a result, stretching does not influence the resistance and thermal current, guaranteeing accurate pressure and temperature sensing. These good sensing behaviors render the MOF-MSMC sensor successfully applied in human healthcare, disease diagnosis, and environmental pressure−temperature dual-modal perception.

RESULTS AND DISCUSSION

Fabrication, Sensing Mechanisms and Characterizations of MOF-MSMC Sensors. The fabrication procedure of the MOF-MSMC sensor is shown in Figure 1a (a detailed description is provided in the Experimental Section). The MOF-MSMC sensors are simply marked as "MOF-MSMC-*t*" (*t* means the growth time) according to their growth time. The MOF-MSMC sensor exhibits good piezoresistive[33] sensing performances (Figure 1b) attributed to the composite film's microstructure provided by MSMC and thermal response behaviors due to the thermoelectric[34] effect of the conductive MOF (Figure 1c, $V_{thermal} = S_T \times \Delta T$, where $V_{thermal}$ is the thermal voltage, S_T is the temperature-sensing sensitivity of the sensor, and ΔT is the temperature gradient across the device). When the sensor is subjected to pressure stimulus, the microstructure of the film is mainly changed, resulting in large relative resistance variations of the sensor but negligible changes in $V_{thermal}$ under the same temperature stimulus. Meanwhile, a temperature stimulus applied at one side of the sensor produces a temperature gradient across the sensor, resulting in the generation of $V_{thermal}$ but limited variation in the relative resistance of the sensor under the same pressure stimulus. On the basis of these two different sensing principles, pressure and temperature stimuli can be distinguishably detected (Figure

1d,e). Given that the MOF-MSMC composite film possesses higher tensile Young's modulus than PDMS,[35] its resistance barely changes under stretch stimulus (Figure 1f).

Figures 1g,h and S1 show that the microstructured, continuous, high-quality, and conductive MOF $Ni_3(HiTP)_2$ film with the conductivity of 4000−5000 S/m[28,29] was successfully prepared. Figure 1i and k display the microstructure of naked MSMC, which is mainly composed of randomly interconnected fibers with the average diameter of 13.2 μm. These fibers make the MSMC surface rough and give it a fluctuation structure with a localized surface roughness of 50.381 nm (Figure S2a). Such rough morphology is beneficial for the growth of $Ni_3(HiTP)_2$. Figure 1j shows that after the growth of $Ni_3(HiTP)_2$ for 5 h, $Ni_3(HiTP)_2$ conformally grows and wraps around the fiber surface, leading to the increase in an average diameter of fibers to 24.8 μm and the formation of a dense, homogeneous, and microstructured $Ni_3(HiTP)_2$ film on the surface of the MSMC membrane. As illustrated in Figure 1l, the $Ni_3(HiTP)_2$ film with a thickness of 245.4 nm tightly adheres onto the MSMC surface. To compare the effect of growth time on the morphology of the MOF-MSMC composite film, MOF-MSMC-2.5h and MOF-MSMC-7.5h composite films were prepared. As shown in Figure S3a−d, both films have less thickness and smaller average fiber diameter and therefore lower conductivity than the MOF-MSMC-5h composite film (Table S1). This may be explained by the fact that $Ni_3(HiTP)_2$ dissolves back to the solution. The film is prepared based on the liquid−solid interfacial growth method. After the film reaches its thickest point at some time, because the film is still in the solution, $Ni_3(HiTP)_2$ originally adhered onto MSMC will dissolve back to the solution. The morphologies of MOF-MSMC composite films with different growth time affect the localized surface roughness (R_a). As shown in Figure S2, the MOF-MSMC-5h composite film possesses the highest localized R_a value of 197.255 nm.

The oxidation stability test (Figure S4) reveals that the resistance of the MOF-MSMC-5h composite film increases by only 0.8-fold when aged in an ambient environment for 3 months, which is better than that of metal, MXene, and organic semiconductors. Figure 1m illustrates the mechanical properties of the naked MSMC substrate and MOF-MSMC-5h composite film. The tensile Young's modulus is 0.35 GPa for the naked MSMC substrate and 1.38 GPa for the MOF-MSMC-5h composite film. Both values are larger than that of PDMS (E_Y of around 1−10 MPa).

Pressure-Sensing Properties of MOF-MSMC Sensors. To investigate the pressure-sensing behaviors, the real-time current (I) under gradually increasing the pressure stimulus was recorded by applying a constant voltage (1 V) across the sensor, and relative current variation was calculated ($\Delta I/I_0$, $\Delta I = I − I_0$,

I_0 refers to the current across the sensor without being pressed, and I stands for the current across the sensor under a pressure stimulus). Sensing range is defined here as the pressure value at which the current across the sensor reaches the saturated state, and GF is the linear slope of the $\Delta I/I_0 - P$ curve.

Figure 2a shows the relative current variation of the MOF-MSMC-5h sensor under a pressure stimulus. Its pressure-sensing range reaches 300 kPa. For sensitivity, the GF values of the MOF-MSMC-5h sensor are as high as 61.61 kPa^{-1} within 32.02 kPa, 10.94 kPa^{-1} ranging from 32.02 to 70.12 kPa, 4.02 kPa^{-1} at the pressure range of 70.12−133.33 kPa, 1.08 kPa^{-1} under the pressure of 133.33−202.10 kPa, and 0.36 kPa^{-1} within the scope of 202.10−300 kPa. Although this performance is inferior to some outstanding reports focused on pure pressure sensing,[36,37] it surpasses most of dual-modal sensors (Figure 2d and Table S3).[22,24,25,30,31,38−47] The fiber-like, rough, and deformable morphology of the Ni$_3$(HiTP)$_2$-MSMC composite film greatly contributes to this desirable performance. To compare the effects of the substrate on the morphology and corresponding pressure-sensing behaviors of the sensor, a polypropylene (PP) membrane was selected as the other substrate and the MOF-PP-5h sensor was produced. Figure S5a illustrates that the MOF-PP-5h composite film is dense, flat, and randomly decorated with a few particles. The cross-sectional view (Figure S5b) indicates that the film thickness is approximately 428 nm. As shown in Figure S6, the pressure-sensing range of the MOF-PP-5h sensor is up to 250 kPa, and its GF values are only 0.40 kPa^{-1} within 30.59 kPa, 0.06 kPa^{-1} under the pressure range of 30.59−106.08 kPa, and 0.01 kPa^{-1} within the scope of 106.08−250 kPa. Due to its flat morphology, the pressure-sensing range and sensitivity of the MOF-PP-5h sensor are inferior to those of the MOF-MSMC-5h sensor. The growth time of Ni$_3$(HiTP)$_2$ onto MSMC affects the morphologies and localized R_a of Ni$_3$(HiTP)$_2$ films, and the corresponding sensors exhibit different pressure-sensing behaviors as plotted in Figure 2b,c. The pressure-sensing behaviors of MOF-MSMC sensors are summarized in Table S2, and the MOF-MSMC-5h sensor shows the best performance because of its lowest film resistance and largest localized R_a that provides the highest initial contact resistance without the pressure stimulus (Table S1 and Figure S2).

On the basis of the above analysis, the MOF-MSMC-5h sensor was chosen as the testing sample to further evaluate other pressure-sensing performances. Figure S7 shows that after experiencing a pressure stimulus of 300 kPa, the MOF-MSMC-5h composite film shows almost no change in morphology, thus guaranteeing the excellent durability of the sensor. As shown in Figure S8, stretch stimulus hardly changes the resistance of the MOF-MSMC-5h composite film owing to the larger tensile Young's modulus of the MOF-MSMC-5h composite film than that of PDMS. Hence, tensile strain is successfully suppressed, which ensures more accuracy of the pressure-sensing compared with other flexible pressure sensors.[36,37,41] To measure the response and recovery time, a sudden pressure (∼5 Pa) was applied to the sensor, maintained for a certain period, and removed quickly from the sensor. In Figure 2e, the response and recovery time of the sensor are both 20 ms. When the pressure was increased to 5, 10, and 50 kPa, the response and recovery time of the sensor are 20, 40, and 40 ms (Figure S9), respectively, all of which are comparable with those of human skin (30−50 ms).[48] The detection limit of the MOF-MSMC-5h sensor was evaluated by applying gradually ascending step pressure (1, 2, and 3 Pa, Figure 2f), and the detection limit can

be as low as 1 Pa, which is much lower than that of human skin (500 Pa).[48,49] Figure S10 elucidates the hysteresis effect of the MOF-MSMC-5h sensor under the first press−release cycle of 300 kPa. The corresponding press and release curves are almost overlapped with the hysteresis value[50] of only 1.8%, indicating the ultralow hysteresis effect of the MOF-MSMC-5h sensor. To measure the sensor's response frequencies, it was loaded with a constant pressure stimulus of 5 kPa with gradually augmented loading frequencies (0.5, 1, 2, and 5 Hz). Figure 2g shows that the pressure-sensing curves are highly consistent under the same frequency and have nearly the same amplitudes under four different frequencies. This finding indicates that the MOF-MSMC-5h sensor is capable of fast and highly synchronous response to high frequency pressure. Figure 2h illustrates the pressure-sensing curves of the MOF-MSMC-5h sensor under gradually increased press stimuli of 0.25, 10, 20, and 30 kPa. The MOF-MSMC-5h sensor exhibits stable and reproducible response to the corresponding pressure. Repeatability is one of the most vital indicators for the sensors' practical use. Under the cyclic pressure stimulus of 10 kPa for 16 000 cycles, the sensor exhibits stable current variation (Figure 2i), although a slight current downshift occurs at primal cycles. Therefore, the prepared sensor has excellent repeatability compared with other pressure sensors.[16,22,24,31,45,46,51,52] The insets of Figure 2i display the current variation of the sensor during the 6200th−6210th cycles (left) and 14540th−14550th cycles (right). The consistent curves confirm the reliable repeatability of the MOF-MSMC-5h sensor and its suitability for practical use in daily life.

Given its excellent pressure-sensing behaviors, the MOF-MSMC-5h sensor can be utilized in human healthcare. For example, owing to its low detection limit and fast response−recovery capabilities, the sensor can monitor subtle pressure signals, such as pulse. Figure 2j,k show the successfully and periodically recorded pulse waves with each composed of percussion peaks (P), tidal peaks (T), and diastolic peaks (D).[53] Therefore, the MOF-MSMC-5h sensor shows application potentials in human daily healthcare. Besides, the MOF-MSMC-5h sensor can be utilized for disease diagnosis. Nowadays, approximately 33% of adults suffer from temporomandibular disorders (TMD), which can cause persistently serious temporomandibular joint pain and even joint dysfunction and pose a huge threat to people's daily life.[54] Anterior disc displacement (ADD) is the most ubiquitous symptom in patients with TMD.[55] Therefore, real-time monitoring of ADD is necessary to prevent TMD deterioration. When people with ADD open their mouths, the condyle beneath the anterior disc will suffer larger pressure[56] from the anterior disc (AD) compared with that of people without ADD. Given its broad pressure-sensing range, the MOF-MSMC-5h sensor can detect the pressure between the condyle and AD. As shown in Figure 2l, animal model experiments were carried out by implanting the sensor (size: 2 mm × 1 mm × 0.4 mm) onto the anterior slope of the condyle of rats. As displayed in Figure 2m, the sensor implanted into the rat with ADD symptoms (marked as "PO") exhibits current variation when the rat opens its mouth. In particular, the change in current increases when the rat widely opens its mouth. However, the sensor implanted into the rat without ADD symptoms (marked as "Sham") exhibits nearly no current change even when the rat opens its mouth. Biocompatibility[57] is one of the most important factors for implanted devices. Hence, biocompatibility experiments were performed separately by implanting MOF-MSMC-PDMS composites and controlled samples into rats. As shown in
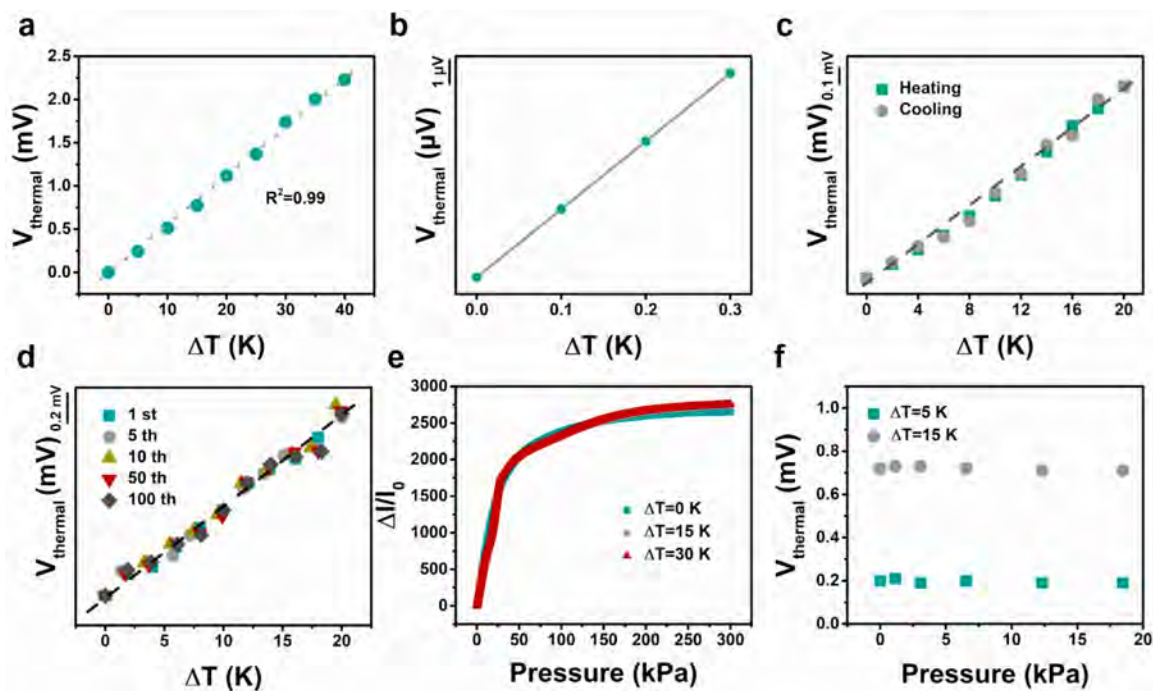
Figure 3. Temperature-sensing behaviors of the MOF-MSMC-5h sensor based on the thermoelectric effect. (a) Output thermal voltage variation *versus* temperature gradient dotted curve of the MOF-MSMC-5h sensor. (b) Output thermal voltage variation of the MOF-MSMC-5h sensor under gradually increasing temperature gradients from 0.1 to 0.3 K. (c) Output thermal voltage variation of the MOF-MSMC-5h sensor under the first heating−cooling cycle under a temperature gradient of 20 K. (d) Output thermal voltage variation of the MOF-MSMC-5h sensor under the 1st, 5th, 10th, 50th, and 100th heating cycle with the temperature gradient of 20 K. (e) Relative current variation *versus* pressure curves of the MOF-MSMC-5h sensor under different temperature gradients of 0, 15, and 30 K. (f) Output thermal voltage variation *versus* pressure dotted curves under constant temperature gradients of 5 K (bottom) and 15 K (top).

Figure S11, no difference is observed in the stained tissues obtained from the rats implanted with MOF-MSMC-PDMS composites and control samples. Besides, in Table S4, the histological evaluation score of the sensor is only 1.67, which can be classified as no inflammatory reaction according to GB/T 16886.6-2015, thus guaranteeing the biocompatibility of the sensor.

Temperature-Sensing Properties of MOF-MSMC Sensors. As a flexible dual-modal sensor, MOF-MSMC-5h shows good temperature-sensing performance due to the thermoelectric effect of conductive MOF $Ni_3(HiTP)_2$. To evaluate the temperature-sensing properties of the MOF-MSMC-5h sensor, real-time thermoelectric voltage ($V_{thermal}$) produced from a temperature gradient stimulus was obtained. For measurement accuracy, the temperature of the unheated side was maintained at 25 °C. Figure 3a presents the relationship between output thermal voltage and temperature gradient from 0 to 40 K. The thermal voltage increases linearly with the applied temperature gradient ΔT within the sensing range of 25−65 °C, which is sufficient for body temperature monitoring. Meanwhile, sensitivity S_T is as high as 57.1 μV/K, which is higher than that of sensors based on PEDOT:PSS,[22,24,25] MXene-AgNW-PEDOT:PSS-PP:TeNW,[32] and graphene.[31] To measure the response and recovery time of temperature sensing, a hot object was quickly put close to one side of the sensor and rapidly removed from the sensor after maintaining for approximately 5 s, during which a real-time thermal voltage variation curve was traced (Figure S12). The response time is 3 s, and the recovery time is 7 s, both of which are larger than those of pressure sensing because of the relatively low thermal diffusivity[58] of $Ni_3(HiTP)_2$. Figure 3b illustrates the thermal voltage variation under subtle

temperature gradients. The temperature resolution is as high as 0.1 K, which is beneficial for the application of the sensor in precise temperature monitoring. Owing to the tensile strain suppression effect, the thermocurrent across the MOF-MSMC-5h composite film is also not influenced by tensile strain (Figure S13). This feature ensures exact results for temperature sensing and is superior to that of other temperature sensors.[13,59−61] A heating−cooling cycle with the stimulus of $\Delta T = 20$ K was applied to the sensor to investigate the hysteresis effect of the temperature sensing of the MOF-MSMC-5h sensor. As illustrated in Figure 3c, the thermal voltage curves under heating and cooling stimuli are almost consistent with each other, revealing a low temperature-sensing hysteresis effect of the MOF-MSMC-5h sensor. Figure 3d plots the temperature-sensing durability results of the sensor ($\Delta T = 20$ K). Under 100 heating cycles, the thermal voltage curves remain highly linear ($R^2 = 0.98−0.99$) and nearly consistent with each other. The integration of these great temperature-sensing properties makes the MOF-MSMC-5h sensor comparable with and even surpass some previously reported flexible temperature sensors (Table S5).[22,24,25,30−32,58,62−64]

Although the MOF-MSMC-5h sensor shows high performance on pressure and temperature sensing, both two sensing functions should be mutually noninterfering to realize its practical use for E-skin. Figure 3e shows that the pressure-sensing curves of the MOF-MSMC-5h sensor under different temperature gradients are nearly overlapped, indicating that its pressure-sensing behaviors are independent of temperature gradients. Additionally, as displayed in Figure 3f, the thermal voltage remains constant under the same temperature gradient but with continuously increasing pressure.
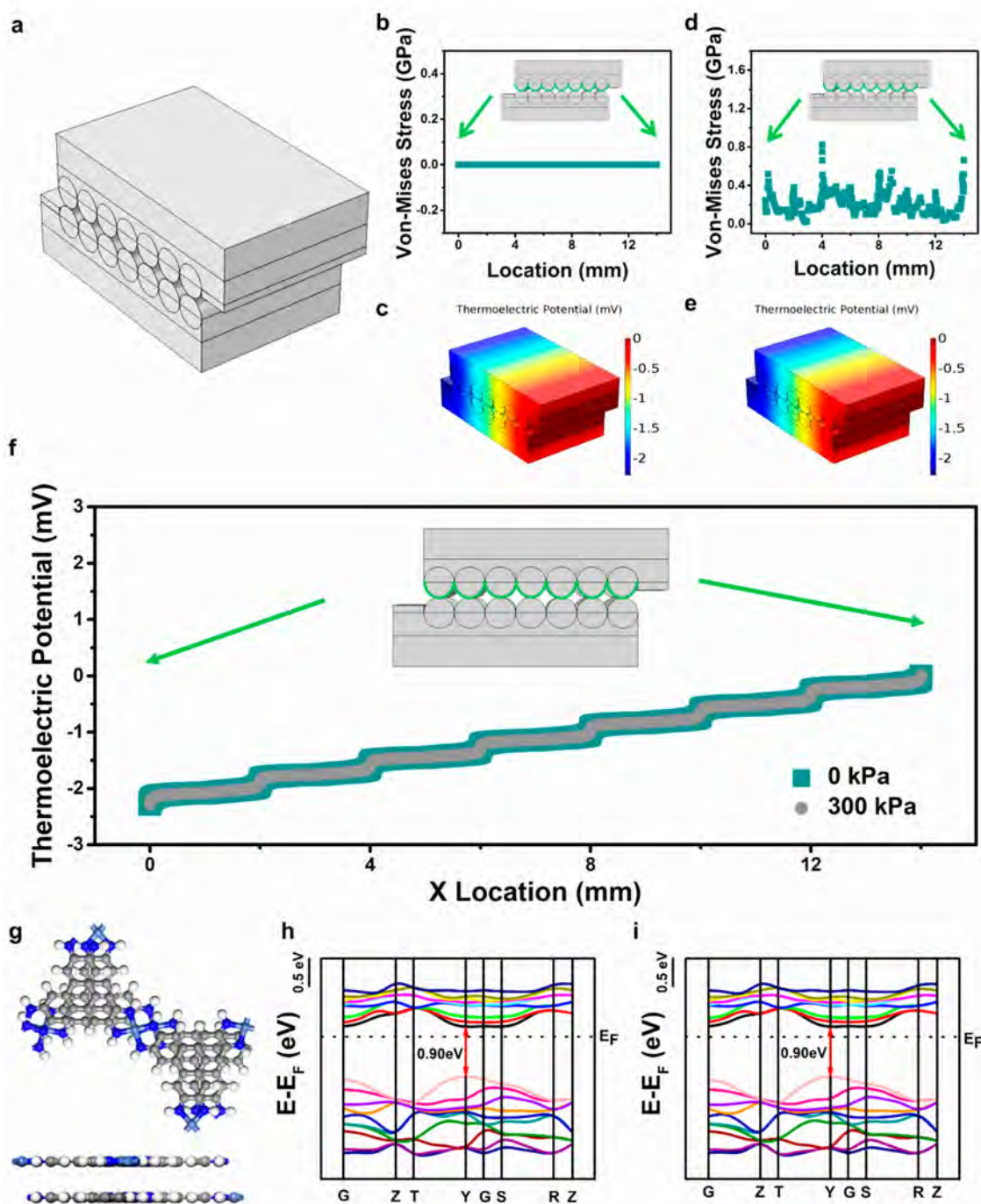
Figure 4. Finite element analysis (FEA) of the sensor under simultaneous temperature and pressure stimulation. (a) FEA model of the sensor. (b) Pressure stress distribution curves at selected districts without input pressure stimulus. (c) Thermal voltage distribution of the sensor under an input temperature gradient stimulus of 40 K but no input pressure stimulus. (d) Pressure stress distribution curves at selected districts under an input pressure stimulus of 300 kPa. (e) Thermal voltage distribution of the sensor under both an input temperature gradient stimulus of 40 K and an input pressure stimulus of 300 kPa. (f) Thermoelectric potential distribution curves at selected districts under different pressure stimuli of 0 and 300 kPa but the same constant temperature gradient stimulus of 40 K. (g−i) First-principles calculation of $Ni_3(HiTP)_2$ under different pressure stimuli. (g) Atomically schematic illustration of $Ni_3(HiTP)_2$ viewed in the vertical direction (top) and front direction (bottom), respectively. (h) Energy band structure of $Ni_3(HiTP)_2$ without pressure. (i) Energy band structure of $Ni_3(HiTP)_2$ under pressure of 300 kPa.

Analysis of the Mutual Noninterference Mechanism of MOF-MSMC Sensors. To verify that thermal voltage is unaffected by pressure, macroscopic finite element analysis (FEA) were carried out. The schematic model is shown in Figure 4a and Table S6. Initially, only a temperature gradient stimulus was applied to one side of the model. As shown in

Figure 4b,c, the contact part of the model is at an unstressed state. Thus, the von Mises Stress at the contact part is 0 Pa (Figure 4b), and the thermal voltage is generated due to the temperature gradient stimulus (Figure 4c). Then, temperature gradient and pressure stimuli were simultaneously applied. Figure 4d shows that because of the pressure stimulus, the
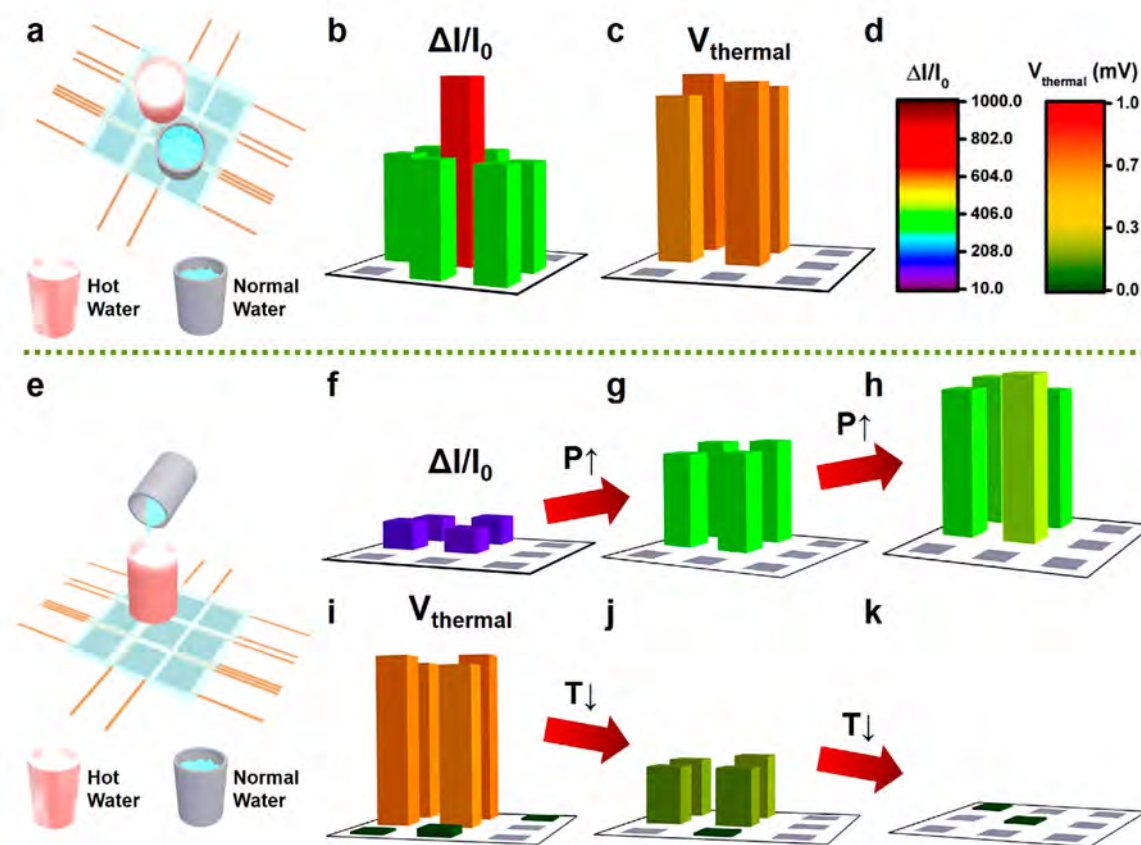
Figure 5. Dual-modal applications of the MOF-MSMC-5h sensor based sensing array. (a) Schematic diagram of the sensing array under simultaneous pressure and temperature stimulation from two bottles of water with the same mass but different temperatures. (b) Corresponding relative current variation of the sensing array under situation (a). (c) Corresponding thermal voltage variation of the sensing array under situation (a). (d) Color scales of the relative current variation (left) from pressure and thermal voltage variation (right) from temperature. (Tips: The color scales are suitable for (b), (c), (f)−(h), and (i)−(k).) (e) Schematic diagram of the sensing array under simultaneous pressure and temperature stimuli by pouring one bottle of water with normal temperature into the other with high temperature on the array. (f−h) Correspondingly relative current variation of the sensing array under two consecutive steps of (e). (i−k) Correspondingly thermal voltage variation of the sensing array under two consecutive steps of (e).

contact part of the model is at a stressed state, and the von Mises Stress at the contact part is nonzero. Thermal voltage is also generated due to the temperature gradient (Figure 4e). Although the contact part of the model is under two different conditions, the thermoelectric potential curves are almost consistent with each other (Figure 4f). Therefore, the thermal voltage of the sensor is unaffected by pressure.

For further explanation, consider the material is subjected to a temperature gradient stimulus, carriers' energy in the heated side changes as reflected in the variation of the energy band. Meanwhile, the carrier's energy in the unheated side remains constant, as indicated by the unchanged state of the energy band. According to thermoelectric physics,[65] these carriers with specific electric charges will migrate from the heated side to the unheated side, leading to the production of thermal voltage. The produced thermal voltage is mainly associated with the carriers' energy difference between the heated and unheated sides. It can be inferred that, if the energy band of the material is hardly affected by pressure, the carriers' energy remains almost unchanged and is mainly affected by temperature. Thus, the thermal voltage mainly depends on the temperature gradient rather than pressure. Microscopic first principles calculations were performed for verification. Figure 4g illustrates the model of MOF $Ni_3(HiTP)_2$, and Figure 4h,i show the calculated energy

band results of MOF $Ni_3(HiTP)_2$ model without a pressure stimulus (Figure 4h) and under a pressure stimulus of 300 kPa (Figure 4i), respectively. The energy band structure curves and band gap values remain nearly consistent with or without pressure stimulus. This finding successfully confirms the above point and reveals the mutual noninterference mechanism between pressure and temperature sensing. Herein, temperature sensing is a reflection of the carriers' energy difference between the heated and unheated sides, and pressure sensing mainly reflects the change in the carriers' migration paths between these two sides. The essence of mutually undisturbed pressure and temperature sensing is that the carriers' energy difference and diffusion paths are mutually noninterfering.

Dual-Modal Applications of the MOF-MSMC Sensor and Its Array. Given its mutually noninterfering dual functions, the MOF-MSMC-5h sensor can be successfully utilized for independent pressure and temperature sensing. When a finger separately presses the left, middle, and right sides of the sensor with gradually increased compression force, the pressure sensing signals are enhanced, but the corresponding thermal voltage values are positive, zero, and negative, respectively (Figure S14a). In addition, the absolute values of the thermal voltage originated from separate contact of the left and right sides from the finger are nearly the same, indicating that the MOF-MSMC-

5h sensor can distinguish the contact location of the thermal source. When different items (finger, pen, and ice) separately come in contact with the left side of the sensor, pressure sensing signals generated from these three items are detected, but thermal voltage signals from only one single the finger and the ice are successfully monitored (Figure S14b). Because the finger, the pen, and the ice have positive, zero, and negative temperature differences with regard to the sensor, thermal voltage signals corresponding to them are positive, zero, and negative, respectively. Therefore, the sensor is capable of simultaneous temperature and pressure sensing without signal disturbance.

Furthermore, a sensing array composed of 3×3 sensing units (Figure S15) was constructed to realize the spatial dual-modal sensing function of E-skin. The corresponding color scales reflecting dual-modal sensing consequences are plotted in Figure 5d. In Figure 5a, two bottles of water with the same mass but different temperatures were placed on different surface locations of the array (one bottle is at room temperature and the other is at high temperature). The spatial distribution results of pressure-sensing signals are consistent with the locations of two bottles (Figure 5b). Nevertheless, the thermal voltage signals can only be detected from where the bottle containing hot water was placed (Figure 5c), thereby confirming that the array can statically distinguish the pressure and temperature distributions of multiple physical stimuli. Moreover, this array is capable of real-time monitoring the dynamical mass and temperature variations. One bottle with hot water was placed on the surface of the array, and the water with room temperature was poured into the bottle containing hot water (Figure 5e). An increase in mass (Figure 5f−h) and a decrease in temperature (Figure 5i−k) are observed clearly. As shown in Figure S14 and Figure 5, this sensor exhibits mutually noninterfering pressure and temperature sensing capabilities and thus has great application potentials in artificially intelligent skin.

CONCLUSION

In conclusion, microstructured, ultrastable, and highly conductive MOF $Ni_3(HiTP)_2$ films were successfully prepared to construct a flexible and strain-suppressed pressure−temperature dual-modal sensor. Owing to its distinct sensing principles, this sensor can independently detect pressure and temperature signals as proved by experimental results and analyzed by theoretical calculations. The MOF-MSMC composite film also suppresses stretch interruptions because its Young's modulus is much larger than that of the PDMS substrate. The sensing performance outperforms that of most of dual-modal sensors. Furthermore, as shown by the successful demonstrations of the sensor and its integrated 3×3 sensing array in environmental perception, this conductive MOF based dual-modal sensor holds great application potentials in high performance and multifunctional flexible E-skin.

EXPERIMENTAL SECTION

Chemicals. All chemicals were purchased through commercial suppliers and used without further purification. Water used in this work was purified using the Milli-Q purification system. Nickel chloride hexahydrate and ammonium hydroxide were purchased from Adamas-beta. 2,3,6,7,10,11-Hexaaminotriphenylene hexahydrochloride was prepared according to the published work.[28]

Preparation of the MOF-MSMC/PP Composite Film. A 10 mg amount of HiTP (2,3,6,7,10,11-hexaaminotriphenylene) and 6.6 mg of nickel(II) chloride hexahydrate were separately dissolved in 10 mL of water. The two solutions were mixed with continuous stirring. 300 μL amount of ammonium hydroxide was added to the above mixture. A MSMC membrane with suitable size was placed on the surface of the solution. After reaction at 65 °C for several hours (2.5, 5, and 7.5 h), the $Ni_3(HiTP)_2$-coated MSMC was washed with ethanol and ultrapure water and then dried under vacuum at 30 °C to yield the MOF-MSMC composite film. The MOF-polypropylene (PP) device was fabricated following the same procedure, except for the use of a PP membrane instead of an MSMC membrane.

Preparation of the MOF-MSMC/PP Sensor. PDMS (Sylgard-184, Dow Corning, a 10:1 mixture of the PDMS prepolymer and curing agent) was prepolymerized by heating at 80 °C for 5 min. Next, the MOF-MSMC composite film was carefully adhered onto the surface of PDMS with the side of MOF exposed to air. Subsequently, the MOF-MSMC composite film with PDMS was completely polymerized at 80 °C for 1 h. After that, one copper conductive wire was installed at one end of the MOF-MSMC device with the assistance of Ag paste. After the Ag paste was dried at room temperature for 1 h, glue was coated around the Ag paste to protect the Ag paste. Finally, the two devices based on MOF-MSMC with PDMS were overlapped with each other to form the MOF-MSMC sensor (the silver paste electrode from one side could not come in contact with the MOF from the other side). The MOF-PP sensor was fabricated according to the same procedure, except the MSMC membrane was substituted by the PP membrane, and the complete polymerization process of PDMS was at room temperature, since the PP membrane featured a heat contraction property, high temperature polymerization seriously broke the structure of the PP membrane, making the MOF-PP composite film lack conductivity. For tensile strain sensing testing, two Cu conductive wires were separately installed at two sides of the MOF-MSMC composite film with the assistance of Ag paste to complete the fabrication of the MOF-MSMC sensor specifically designed for tensile strain sensing testing (also, after the Ag paste was dried at room temperature for 1 h, glue was coated around the Ag paste to protect the Ag paste).

Animal Experiments. Eight-week-old male Sprague−Dawley rats (280−300 g) were purchased from Vital River Laboratory. The study was authorized by the Peking University Animal Ethics Committee. Rats were anesthetized by intraperitoneally injecting 1% pentobarbital sodium. Under sterile surgical conditions, the right temporomandibular joint (TMJ) was exposed. In the experimental group, to induce TMJ osteoarthritis, a needle with 5−0 suture was passed through the posterior of the disc vertically and was fixed to the bend point of the zygomatic arch, which displaced the disc from the upper surface of the condyle to the anterior surface of the condyle. In the control group, the disc was separated from the condyle but not displaced. Then the sterile implant (MOF-MSMC-5h sensor sealed by PDMS, size: 2 mm × 1 mm × 0.7 mm) was placed and stuck on the anterior surface of the condyle by medical gum (Campaign, China). The incision was closed. The changes of pressure on the anterior surface of the condyle were monitored during passive opening and closing movements of the mandible in rats under anesthesia.

Characterizations and Measurements. The phase composition and crystalline structure of the sample were characterized by a high-resolution multifunction X-ray diffractometer (D8 Discover Davinci, German). The morphologies of the samples were characterized by FE-SEM (Hitachi SU8220, Japan). Image-Pro-Plus 6 was utilized for the quantitative analysis of the SEM images. The oxidation stability properties of the MOF-MSMC composite film were separately characterized by putting the device in the air (room temperature) and the oven (80 °C) for several months to measure the resistance variation with the assistance of a digital multimeter (FLUKE-15B). The pressure-sensing-related properties of the MOF-based sensors were measured by using the system composed of a high-precision electronic universal testing machine (CMT6103, MTS Systems (China) Co., Ltd.) connected with a customized force gauge (high-pressure range: Mark-10 and M5-20 force gauge, low-pressure range: MSMC) to provide a pressure stimulus and record real-time pressure signals, an electrochemical station (PARSTAT 2273 Princeton Applied Research) to provide a constant voltage (1 V), and a software system to record

real-time current signals under continuous pressure stimuli. The contact area was calculated on the basis of the overlapped surface of the MOF-MSMC composite films. The tensile-sensing-related property of the MOF-MSMC composite film was measured by using the system composed of a high-precision motorization linear stage (a displacement resolution of 2.5 μm) for the application of tensile strain, an electrochemical station (PARSTAT 2273 Princeton Applied Research) to provide a constant voltage (1 V), and a software system to record real-time current signals under a stretching stimulus. The temperature-sensing related properties of the MOF based sensors were measured by using two parallelly connected Peltier TE modules put under the sensors to create a temperature gradient field across the sensors in a left−right direction, a digital thermocouple with two probes separately contacting the surface of two sides of PDMS placed between two Peltier TE modules to accurately record the real-time temperature variation of the sensors, and a Keithley 2400 system controlled by a computer to record real-time thermal current and thermal voltage signals under a temperature stimulus.

Macroscopic FEA Model and Microscopic First-Principles Calculations. The finite element analysis were carried out by using the software COMSOL Multiphysics 5.3a to analyze the thermal potential distribution of the MOF-based sensors under pressure of 0 and 300 kPa. The model-related parameters are listed in Table S6 in detail. The first principles calculations were carried out by using the Castep Module in Materials Studio 2017R2 to calculate the band structures of MOF under 0 and 300 kPa. At the beginning, the MOF crystals were geometrically optimized, and band structures were calculated by using the GGA-PBE function combined with an OTFG ultrasoft pseudopotential, with the cutoff energy of 500 eV and k-grids of $2 \times 2 \times 1$. Tolerance was set at 2×10^{-5} eV.

ASSOCIATED CONTENT

Ⓢ Supporting Information

The Supporting Information is available free of charge at https://pubs.acs.org/doi/10.1021/acsnano.1c07388.

XRD pattern of the MOF-MSMC-5h composite film; localized 2D surface profiling images of the naked MSMC and MOF-MSMC composite films; SEM morphologies of the MOF-MSMC and MOF-PP-5h composite films; antioxidation stability of the MOF-MSMC-5h composite film; pressure-sensing curve of the MOF-PP-5h sensor; SEM morphologies of the MOF-MSMC-5h composite film before and after being pressed; strain-sensing curve of one part of the MOF-MSMC-5h sensor; relative current variation of the MOF-MSMC-5h sensor under various pressure stimuli; pressure-sensing curves of the MOF-MSMC-5h sensor under press−release cycle; optical image of the stained tissue of rats; output thermal voltage variation of the MOF-MSMC-5h sensor under a quasi-transient temperature gradient stimulus; relative thermal current variation *versus* strain dotted curves of the MOF-MSMC-5h composite film; dual-functional applications of one single MOF-MSMC-5h sensor; optical image of the 3×3 MOF-MSMC-5h sensor array; comparison of the initial average resistance of MOF-MSMC composite films and the corresponding sensors without pressure stimulus; summary of the pressure-sensing results of MOF-MSMC sensors; comparison of pressure- and temperature-sensing results with previously reported sensors; evaluation summary of biocompatibility; macroscopic FEA model simulation information (PDF)

AUTHOR INFORMATION

Corresponding Authors

Ranran Wang − *State Key Laboratory of High Performance Ceramics and Superfine Microstructure, Shanghai Institute of Ceramics, Chinese Academy of Sciences, Shanghai 200050, China; School of Chemistry and Materials Science, Hangzhou Institute for Advanced Study, University of Chinese Academy of Sciences, Hangzhou 310024, China;* Email: wangranran@mail.sic.ac.cn

Guan-E Wang − *State Key Laboratory of Structural Chemistry, Fujian Institute of Research on the Structure of Matter, Chinese Academy of Sciences, Fuzhou 350002, China;* Email: gewang@fjirsm.ac.cn

Jing Sun − *State Key Laboratory of High Performance Ceramics and Superfine Microstructure, Shanghai Institute of Ceramics, Chinese Academy of Sciences, Shanghai 200050, China;* orcid.org/0000-0003-1101-1584; Email: jingsun@mail.sic.ac.cn

Authors

Yuxiang Li − *State Key Laboratory of High Performance Ceramics and Superfine Microstructure, Shanghai Institute of Ceramics, Chinese Academy of Sciences, Shanghai 200050, China; Center of Materials Science and Optoelectronics Engineering, University of Chinese Academy of Sciences, Beijing 100049, China*

Shiyang Feng − *Central Laboratory, Peking University School and Hospital of Stomatology, Beijing 100081, China; National Clinical Research Center for Oral Diseases, Beijing 100081, China*

Wenge Shi − *Central Laboratory, Peking University School and Hospital of Stomatology, Beijing 100081, China; National Clinical Research Center for Oral Diseases, Beijing 100081, China*

Yin Cheng − *State Key Laboratory of High Performance Ceramics and Superfine Microstructure, Shanghai Institute of Ceramics, Chinese Academy of Sciences, Shanghai 200050, China*

Liangjing Shi − *State Key Laboratory of High Performance Ceramics and Superfine Microstructure, Shanghai Institute of Ceramics, Chinese Academy of Sciences, Shanghai 200050, China*

Kaiyuan Fu − *Central Laboratory, Peking University School and Hospital of Stomatology, Beijing 100081, China; National Clinical Research Center for Oral Diseases, Beijing 100081, China*

Complete contact information is available at:
https://pubs.acs.org/10.1021/acsnano.1c07388

Author Contributions

Y.L., R.W., and G.-E.W. planned and designed the project. Y.L. and R.W. conducted all of the experiments, analyzed the data, and wrote paper. G.-E.W. helped to synthesize the materials and characterize the samples. S.F., W.S., and K.F. conducted the animal experiments. L.S. and Y.C. helped to do experiments. J.S. supervised the project.

Notes

The authors declare no competing financial interest.

REFERENCES

(1) Gao, W.; Ota, H.; Kiriya, D.; Takei, K.; Javey, A. Flexible Electronics toward Wearable Sensing. *Acc. Chem. Res.* **2019**, *52*, 523−533.

(2) Pang, Y.; Yang, Z.; Yang, Y.; Ren, T. L. Wearable Electronics Based on 2D Materials for Human Physiological Information Detection. *Small* **2020**, *16*, 1901124.

(3) Wang, C. Y.; Xia, K. L.; Wang, H. M.; Liang, X. P.; Yin, Z.; Zhang, Y. Y. Advanced Carbon for Flexible and Wearable Electronics. *Adv. Mater.* **2019**, *31*, 1801072.

(4) Hou, C.; Wang, H.; Zhang, Q.; Li, Y.; Zhu, M. Highly Conductive, Flexible, and Compressible All-Graphene Passive Electronic Skin for Sensing Human Touch. *Adv. Mater.* **2014**, *26*, 5018−5024.

(5) Cheng, Y.; Lu, X.; Hoe Chan, K.; Wang, R.; Cao, Z.; Sun, J.; Wei Ho, G. A Stretchable Fiber Nanogenerator for Versatile Mechanical Energy Harvesting and Self-Powered Full-Range Personal Healthcare Monitoring. *Nano Energy* **2017**, *41*, 511−518.

(6) Shan, G. C.; Li, X.; Huang, W. AI-Enabled Wearable and Flexible Electronics for Assessing Full Personal Exposures. *Innovation* **2020**, *1*, 100031.

(7) Xie, M. Y.; Hisano, K.; Zhu, M. Z.; Toyoshi, T.; Pan, M.; Okada, S.; Tsutsumi, O.; Kawamura, S.; Bowen, C. Flexible Multifunctional Sensors for Wearable and Robotic Applications. *Adv. Mater. Technol.* **2019**, *4*, 1800626.

(8) Zhao, D.; Zhu, Y.; Cheng, W.; Chen, W.; Wu, Y.; Yu, H. Cellulose-Based Flexible Functional Materials for Emerging Intelligent Electronics. *Adv. Mater.* **2021**, *33*, 2000619.

(9) Yang, Y. N.; Wang, R. R.; Sun, J. MXenes in Flexible Force Sensitive Sensors: A Review. *J. Inorg. Mater.* **2020**, *35*, 8−18.

(10) Zhang, H.; Han, W.; Xu, K.; Zhang, Y.; Lu, Y.; Nie, Z.; Du, Y.; Zhu, J.; Huang, W. Metallic Sandwiched-Aerogel Hybrids Enabling Flexible and Stretchable Intelligent Sensor. *Nano Lett.* **2020**, *20*, 3449−3458.

(11) Zhai, L.; Narkar, A.; Ahn, K. Self-Healing Polymers with Nanomaterials and Nanostructures. *Nano Today* **2020**, *30*, 100826.

(12) Gao, Y. J.; Ota, H.; Schaler, E. W.; Chen, K.; Zhao, A.; Gao, W.; Fahad, H. M.; Leng, Y. G.; Zheng, A. Z.; Xiong, F. R.; Zhang, C. C.; Tai, L. C.; Zhao, P. D.; Fearing, R. S.; Javey, A. Wearable Microfluidic Diaphragm Pressure Sensor for Health and Tactile Touch Monitoring. *Adv. Mater.* **2017**, *29*, 1701985.

(13) Yokota, T.; Inoue, Y.; Terakawa, Y.; Reeder, J.; Kaltenbrunner, M.; Ware, T.; Yang, K.; Mabuchi, K.; Murakawa, T.; Sekino, M.; Voit, W.; Sekitani, T.; Someya, T. Ultraflexible, Large-Area, Physiological Temperature Sensors for Multipoint Measurements. *Proc. Natl. Acad. Sci. U. S. A.* **2015**, *112*, 14533−14538.

(14) Li, Q.; Zhang, L. N.; Tao, X. M.; Ding, X. Review of Flexible Temperature Sensing Networks for Wearable Physiological Monitoring. *Adv. Healthcare Mater.* **2017**, *6*, 1601371.

(15) Hong, S. Y.; Lee, Y. H.; Park, H.; Jin, S. W.; Jeong, Y. R.; Yun, J.; You, I.; Zi, G.; Ha, J. S. J. A. n. Stretchable Active Matrix Temperature Sensor Array of Polyaniline Nanofibers for Electronic Skin. *Adv. Mater.* **2016**, *28*, 930−935.

(16) Hua, Q.; Sun, J.; Liu, H.; Bao, R.; Yu, R.; Zhai, J.; Pan, C.; Wang, Z. L. Skin-Inspired Highly Stretchable and Conformable Matrix Networks for Multifunctional Sensing. *Nat. Commun.* **2018**, *9*, 244.

(17) Ho, D. H.; Sun, Q.; Kim, S. Y.; Han, J. T.; Kim, D. H.; Cho, J. H. Stretchable and Multimodal All Graphene Electronic Skin. *Adv. Mater.* **2016**, *28*, 2601−2608.

(18) Nguyen Thanh, T.; Jeon, S.; Kim, D.-I.; Tran Quang, T.; Jang, M.; Hwang, B.-U.; Byun, K.-E.; Bae, J.; Lee, E.; Tok, J. B. H.; Bao, Z.; Lee, N.-E.; Park, J.-J. A Flexible Bimodal Sensor Array for Simultaneous Sensing of Pressure and Temperature. *Adv. Mater.* **2014**, *26*, 796−804.

(19) Ota, H.; Chen, K.; Lin, Y.; Kiriya, D.; Shiraki, H.; Yu, Z.; Ha, T.-J.; Javey, A. Highly Deformable Liquid-State Heterojunction Sensors. *Nat. Commun.* **2014**, *5*, 5032.

(20) Song, K.; Zhao, R. D.; Wang, Z. L.; Yang, Y. Conjuncted Pyro-Piezoelectric Effect for Self-Powered Simultaneous Temperature and Pressure Sensing. *Adv. Mater.* **2019**, *31*, 1902831.

(21) Liu, K.; Zhou, Y. S.; Yuan, F.; Mo, X. B.; Yang, P. H.; Chen, Q.; Li, J.; Ding, T. P.; Zhou, J. Self-Powered Multimodal Temperature and Force Sensor Based on a Liquid Droplet. *Angew. Chem., Int. Ed.* **2016**, *55*, 15864−15868.

(22) Zhang, F.; Zang, Y.; Huang, D.; Di, C. A.; Zhu, D. Flexible and Self-Powered Temperature-Pressure Dual-Parameter Sensors Using Microstructure-Frame-Supported Organic Thermoelectric Materials. *Nat. Commun.* **2015**, *6*, 8356.

(23) You, I.; Mackanic, D. G.; Matsuhisa, N.; Kang, J.; Kwon, J.; Beker, L.; Mun, J.; Suh, W.; Kim, T. Y.; Tok, J. B. H.; Bao, Z. N.; Jeong, U. Artificial Multimodal Receptors Based on Ion Relaxation Dynamics. *Science* **2020**, *370*, 961−965.

(24) Han, S. B.; Alvi, N. U.; Granlof, L.; Granberg, H.; Berggren, M.; Fabiano, S.; Crispin, X. A Multiparameter Pressure-Temperature-Humidity Sensor Based on Mixed Ionic-Electronic Cellulose Aerogels. *Adv. Sci.* **2019**, *6*, 1802128.

(25) Han, S. B.; Jiao, F.; Khan, Z. U.; Edberg, J.; Fabiano, S.; Crispin, X. Thermoelectric Polymer Aerogels for Pressure-Temperature Sensing Applications. *Adv. Funct. Mater.* **2017**, *27*, 1703549.

(26) Sun, L.; Campbell, M. G.; Dinca, M. Electrically Conductive Porous Metal-Organic Frameworks. *Angew. Chem., Int. Ed.* **2016**, *55*, 3566−3579.

(27) Zang, Y.; Pei, F.; Huang, J. H.; Fu, Z. H.; Xu, G.; Fang, X. L. Large-Area Preparation of Crack-Free Crystalline Microporous Conductive Membrane to Upgrade High Energy Lithium-Sulfur Batteries. *Adv. Energy Mater.* **2018**, *8*, 1802052.

(28) Sheberla, D.; Sun, L.; Blood-Forsythe, M. A.; Er, S.; Wade, C. R.; Brozek, C. K.; Aspuru-Guzik, A.; Dinca, M. High Electrical Conductivity in $Ni_3(2,3,6,7,10,11-Hexaiminotriphenylene)_2$, a Semiconducting Metal-Organic Graphene Analogue. *J. Am. Chem. Soc.* **2014**, *136*, 8859−8862.

(29) Day, R. W.; Bediako, D. K.; Rezaee, M.; Parent, L. R.; Skorupskii, G.; Arguilla, M. Q.; Hendon, C. H.; Stassen, I.; Gianneschi, N. C.; Kim, P.; Dinca, M. Single Crystals of Electrically Conductive Two-Dimensional Metal-Organic Frameworks: Structural and Electrical Transport Properties. *ACS Cent. Sci.* **2019**, *5*, 1959−1964.

(30) Wang, Y. L.; Mao, H. Y.; Wang, Y.; Zhu, P. C.; Liu, C. H.; Deng, Y. 3D Geometrically Structured PANI/CNT-Decorated Polydimethylsiloxane Active Pressure and Temperature Dual-Parameter Sensors for Man-Machine Interaction Applications. *J. Mater. Chem. A* **2020**, *8*, 15167−15176.

(31) Wang, Y.; Wu, H. T.; Xu, L.; Zhang, H. N.; Yang, Y.; Wang, Z. L. Hierarchically Patterned Self-Powered Sensors for Multifunctional Tactile Sensing. *Sci. Adv.* **2020**, *6*, No. eabb9083.

(32) Li, F. C.; Liu, Y.; Shi, X. L.; Li, H. P.; Wang, C. H.; Zhang, Q.; Ma, R. J.; Liang, J. J. Printable and Stretchable Temperature-Strain Dual-Sensing Nanocomposite with High Sensitivity and Perfect Stimulus Discriminability. *Nano Lett.* **2020**, *20*, 6176−6184.

(33) Liu, W.; Liu, N.; Yue, Y.; Rao, J.; Cheng, F.; Su, J.; Liu, Z.; Gao, Y. Piezoresistive Pressure Sensor Based on Synergistical Innerconnect Polyvinyl Alcohol Nanowires/Wrinkled Graphene Film. *Small* **2018**, *14*, 1704149.

(34) Zhang, D.; Wang, Y.; Yang, Y. Design, Performance, and Application of Thermoelectric Nanogenerators. *Small* **2019**, *15*, 1805241.

(35) Zhu, C.; Chortos, A.; Wang, Y.; Pfattner, R.; Lei, T.; Hinckley, A. C.; Pochorovski, I.; Yan, X.; To, J. W. F.; Oh, J. Y.; Tok, J. B. H.; Bao, Z.; Murmann, B. Stretchable Temperature-Sensing Circuits with Strain Suppression Based on Carbon Nanotube Transistors. *Nat. Electron.* **2018**, *1*, 183−190.

(36) Bai, N.; Wang, L.; Wang, Q.; Deng, J.; Wang, Y.; Lu, P.; Huang, J.; Li, G.; Zhang, Y.; Yang, J.; Xie, K.; Zhao, X.; Guo, C. F. Graded

Intrafillable Architecture-Based Iontronic Pressure Sensor with Ultra-Broad-Range High Sensitivity. *Nat. Commun.* **2020**, *11*, 209.

(37) Lee, Y.; Myoung, J.; Cho, S.; Park, J.; Kim, J.; Lee, H.; Lee, Y.; Lee, S.; Baig, C.; Ko, H. Bioinspired Gradient Conductivity and Stiffness for Ultrasensitive Electronic Skins. *ACS Nano* **2021**, *15*, 1795−1804.

(38) Fu, X.; Dong, H.; Zhen, Y.; Hu, W. Solution-Processed Large-Area Nanocrystal Arrays of Metal-Organic Frameworks as Wearable, Ultrasensitive, Electronic Skin for Health Monitoring. *Small* **2015**, *11*, 3351−3356.

(39) Wang, K.; Lou, Z.; Wang, L.; Zhao, L.; Zhao, S.; Wang, D.; Han, W.; Jiang, K.; Shen, G. Bioinspired Interlocked Structure-Induced High Deformability for Two-Dimensional Titanium Carbide (MXene)/Natural Microcapsule-Based Flexible Pressure Sensors. *ACS Nano* **2019**, *13*, 9139−9147.

(40) Tao, L. Q.; Zhang, K. N.; Tian, H.; Liu, Y.; Wang, D. Y.; Chen, Y. Q.; Yang, Y.; Ren, T. L. Graphene-Paper Pressure Sensor for Detecting Human Motions. *ACS Nano* **2017**, *11*, 8790−8795.

(41) Qiu, Z.; Wan, Y.; Zhou, W.; Yang, J.; Yang, J.; Huang, J.; Zhang, J.; Liu, Q.; Huang, S.; Bai, N.; Wu, Z.; Hong, W.; Wang, H.; Guo, C. F. Ionic Skin with Biomimetic Dielectric Layer Templated from *Calathea Zebrine* Leaf. *Adv. Funct. Mater.* **2018**, *28*, 1802343.

(42) Gao, Y.; Yan, C.; Huang, H.; Yang, T.; Tian, G.; Xiong, D.; Chen, N.; Chu, X.; Zhong, S.; Deng, W.; Fang, Y.; Yang, W. Microchannel-Confined MXene Based Flexible Piezoresistive Multifunctional Micro-Force Sensor. *Adv. Funct. Mater.* **2020**, *30*, 1909603.

(43) Zou, B. H.; Chen, Y. Y.; Liu, Y. H.; Xie, R. J.; Du, Q. J.; Zhang, T.; Shen, Y.; Zheng, B.; Li, S.; Wu, J. S.; Zhang, W. N.; Huang, W.; Huang, X.; Huo, F. W. Repurposed Leather with Sensing Capabilities for Multifunctional Electronic Skin. *Adv. Sci.* **2019**, *6*, 1801283.

(44) Ma, Y.; Liu, N.; Li, L.; Hu, X.; Zou, Z.; Wang, J.; Luo, S.; Gao, Y. A Highly Flexible and Sensitive Piezoresistive Sensor Based on MXene with Greatly Changed Interlayer Distances. *Nat. Commun.* **2017**, *8*, 1207.

(45) Lee, S.; Franklin, S.; Hassani, F. A.; Yokota, T.; Nayeem, O. G.; Wang, Y.; Leib, R.; Cheng, G.; Franklin, D. W.; Someya, T. Nanomesh Pressure Sensor for Monitoring Finger Manipulation without Sensory Interference. *Science* **2020**, *370*, 966−970.

(46) Zhang, Y.; Wang, L.; Zhao, L.; Wang, K.; Zheng, Y.; Yuan, Z.; Wang, D.; Fu, X.; Shen, G.; Han, W. Flexible Self-Powered Integrated Sensing System with 3D Periodic Ordered Black Phosphorus@MXene Thin-Films. *Adv. Mater.* **2021**, *33*, 2007890.

(47) Lee, Y.; Park, J.; Cho, S.; Shin, Y. E.; Lee, H.; Kim, J.; Myoung, J.; Cho, S.; Kang, S.; Baig, C.; Ko, H. Flexible Ferroelectric Sensors with Ultrahigh Pressure Sensitivity and Linear Response over Exceptionally Broad Pressure Range. *ACS Nano* **2018**, *12*, 4045−4054.

(48) Hammock, M. L.; Chortos, A.; Tee, B. C. K.; Tok, J. B. H.; Bao, Z. 25th Anniversary Article: The Evolution of Electronic Skin (E-Skin): A Brief History, Design Considerations, and Recent Progress. *Adv. Mater.* **2013**, *25*, 5997−6037.

(49) Chortos, A.; Bao, Z. Skin-Inspired Electronic Devices. *Mater. Today* **2014**, *17*, 321−331.

(50) Wang, Y.; Jia, Y.; Zhou, Y.; Wang, Y.; Zheng, G.; Dai, K.; Liu, C.; Shen, C. Ultra-Stretchable, Sensitive and Durable Strain Sensors Based on Polydopamine Encapsulated Carbon Nanotubes/Elastic Bands. *J. Mater. Chem. C* **2018**, *6*, 8160−8170.

(51) Zhou, K.; Zhang, C.; Xiong, Z.; Chen, H.-Y.; Li, T.; Ding, G.; Yang, B.; Liao, Q.; Zhou, Y.; Han, S.-T. Template-Directed Growth of Hierarchical MOF Hybrid Arrays for Tactile Sensor. *Adv. Funct. Mater.* **2020**, *30*, 2001296.

(52) Zhao, X.-F.; Hang, C.-Z.; Lu, H.-L.; Xu, K.; Zhang, H.; Yang, F.; Ma, R.-G.; Wang, J.-C.; Zhang, D. W. A Skin-Like Sensor for Intelligent Braille Recognition. *Nano Energy* **2020**, *68*, 104346.

(53) Nie, P.; Wang, R.; Xu, X.; Cheng, Y.; Wang, X.; Shi, L.; Sun, J. High-Performance Piezoresistive Electronic Skin with Bionic Hierarchical Microstructure and Microcracks. *ACS Appl. Mater. Interfaces* **2017**, *9*, 14911−14919.

(54) Nota, A.; Ryakhovsky, A. N.; Bosco, F.; Tecco, S. A Full Digital Workflow to Design and Mill a Splint for a Patient with Temporomandibular Joint Disorder. *Appl. Sci.* **2021**, *11*, 372.

(55) Shen, P.; Chen, X.; Xie, Q.; Zhang, S.; Yang, C. Assessment of Occlusal Appliance for the Reposition of Temporomandibular Joint Anterior Disc Displacement with Reduction. *J. Craniofac.Surg.* **2019**, *30*, 1140−1143.

(56) Zhang, S.; Huang, D.; Liu, X.; Yang, C.; Undt, G.; Haddad, S. M.; Chen, Z. Arthroscopic Treatment for Intra-Articular Adhesions of the Temporomandibular Joint. *J. Oral Maxillofac.Surg.* **2011**, *69*, 2120−2127.

(57) Cheng, Y.; Wang, R.; Sun, J.; Gao, L. Highly Conductive and Ultrastretchable Electric Circuits from Covered Yarns and Silver Nanowires. *ACS Nano* **2015**, *9*, 3887−3895.

(58) Zhu, P. C.; Wang, Y.; Sheng, M.; Wang, Y. L.; Yu, Y. D.; Deng, Y. A Flexible Active Dual-Parameter Sensor for Sensitive Temperature and Physiological Signal Monitoring *via* Integrating Thermoelectric and Piezoelectric Conversion. *J. Mater. Chem. A* **2019**, *7*, 8258−8267.

(59) Ge, G.; Lu, Y.; Qu, X.; Zhao, W.; Ren, Y.; Wang, W.; Wang, Q.; Huang, W.; Dong, X. Muscle-Inspired Self-Healing Hydrogels for Strain and Temperature Sensor. *ACS Nano* **2020**, *14*, 218−228.

(60) Ye, Y.; Zhang, Y.; Chen, Y.; Han, X.; Jiang, F. Cellulose Nanofibrils Enhanced, Strong, Stretchable, Freezing-Tolerant Ionic Conductive Organohydrogel for Multi-Functional Sensors. *Adv. Funct. Mater.* **2020**, *30*, 2003430.

(61) Wu, X. D.; Zhu, J.; Evans, J. W.; Lu, C. H.; Arias, A. C. A Potentiometric Electronic Skin for Thermosensation and Mechano-sensation. *Adv. Funct. Mater.* **2021**, *31*, 2010824.

(62) Wang, Q.; Ling, S.; Liang, X.; Wang, H.; Lu, H.; Zhang, Y. Self-Healable Multifunctional Electronic Tattoos Based on Silk and Graphene. *Adv. Funct. Mater.* **2019**, *29*, 1808695.

(63) Cao, Z.; Yang, Y.; Zheng, Y.; Wu, W.; Xu, F.; Wang, R.; Sun, J. Highly Flexible and Sensitive Temperature Sensors Based on $Ti_3C_2T_x$ (MXene) for Electronic Skin. *J. Mater. Chem. A* **2019**, *7*, 25314−25323.

(64) Bang, J.; Lee, W. S.; Park, B.; Joh, H.; Woo, H. K.; Jeon, S.; Ahn, J.; Jeong, C.; Kim, T. I.; Oh, S. J. Highly Sensitive Temperature Sensor: Ligand-Treated Ag Nanocrystal Thin Films on PDMS with Thermal Expansion Strategy. *Adv. Funct. Mater.* **2019**, *29*, 1903047.

(65) Shakouri, A. Recent Developments in Semiconductor Thermoelectric Physics and Materials. *Annu. Rev. Mater. Res.* **2011**, *41*, 399−431.